Submodule Switching-State Based EMI Modeling and Mixed-Mode EMI Phenomenon in MMC

Tao Sun, Xuejun Pei, *Senior Member, IEEE*, Yue Shan, Jian'guo Pei, and Dong Jiang, *Senior Member, IEEE*

***Abstract*—Modular multilevel converter (MMC) is widely used in high-voltage occasions for its good power qualities and flexible controls. However, the large number of semiconductor switches would lead to an extremely complicated electromagnetic environment. To clarify the detailed conducted electromagnetic interference (EMI) mechanisms of MMC, this article builds an EMI model of MMC considering different submodule switching states. Based on this model, the EMI paths of submodule switching-ON and switching-OFF processes are analyzed. Then, this article analyzes the effects of submodule heatsink connecting patterns on EMI, and explains the mechanisms of mixed-mode (MM) EMI phenomenon that common-mode component brings in extra differential-mode component. Simulation and experiment results verify the proposed EMI mechanisms and MM phenomenon. The conclusions of this article have great reference significance for the EMI research of MMC and other high-voltage converters.**

***Index Terms*—Electromagnetic interference (EMI) model, heatsink connecting patterns, mixed-mode (MM) EMI phenomenon, modular multilevel converter (MMC), submodule switching states.**

I. Introduction

MODULAR multilevel converter (MMC), which was first proposed by Professor R. Marquardt in 2001 [1], has become the most widely used multilevel converter in the high-voltage direct current transmission system so far. MMC not only has the common advantages of multilevel converters (high-power qualities, low switching losses, flexible control freedoms, etc.), but also owns its unique advantage of modularization [2], [3]. The existing researches of MMC are most focused on the circuit topology, modulation methods, control strategies, circulating current suppression, capacitor voltage balance, fault ride-through, etc., while the potential electromagnetic interference (EMI) problems are rarely noticed. This is because that people are usually more concerned about the external performance of output qualities, while MMC is doing well in this regard.

Manuscript received 28 April 2022; revised 20 July 2022 and 23 August 2022; accepted 1 October 2022. Date of publication 17 October 2022; date of current version 18 November 2022. This work was supported in part by the National Natural Science Foundation of China under Grant U1866211, and in part by the National Natural Science Foundation of China under Grant 51977091. Recommended for publication by Associate Editor F. Costa. *(Corresponding authors: Dong Jiang; Xuejun Pei.)*

The authors are with the State Key Laboratory of Advanced Electromagnetic Engineering and Technology, School of Electrical and Electronic Engineering, Huazhong University of Science and Technology, Wuhan 430074, China (e-mail: d202080595@hust.edu.cn; ppei215@mail.hust.edu.cn; yueshan@hust.edu.cn; husterpjg@foxmail.com; jiangd@hust.edu.cn).

Color versions of one or more figures in this article are available at https://doi.org/10.1109/TPEL.2022.3214990.

Digital Object Identifier 10.1109/TPEL.2022.3214990

For a huge complicated power electronic system like MMC, its internal EMI problems may be very serious [4], [5], [6], [7]. The utilization of large number of semiconductor switches in MMC brings a lot of potential EMI sources into the system, forming an extremely complex electromagnetic environment. On the one hand, the generated EMI may interfere with the regular functions of the electronic system, such as sampling, communication, control, driver, and relaying protection. On the other hand, the overlarge EMI level also threatens the safety of workers and equipment outside the valve tower [4]. In order to avoid the possible EMI faults to the maximum extent, some relative measures must be taken in practical engineering projects. However, the existing industrial EMI standards and engineering experiences are more focused on solving the EMI emission and immunity problems, while neglecting the EMI interactions inside devices. This may result in that EMI faults still occur even when necessary EMI suppression measures have been taken. To solve this problem fundamentally, a deep exploration of EMI propagation mechanisms should be made.

The conducted EMI generated by high-voltage circuits may interfere with the regular operations of electronic circuits. For example, the noise current from the main circuit may flow into auxiliary power supplies through submodule capacitors and generate EMI in the power supply circuits [7]. To figure out the conducted EMI mechanisms of MMC, scholars have made some efforts. In the aspect of EMI modeling, Chen et al. [7] built a common-mode (CM) EMI model for submodule auxiliary power supply. The staircase wave based EMI source modeling method for single-phase MMC was proposed in [8], [9], and [10]. However, this method did not show how EMI propagates in submodules and it is differential-mode (DM) model, to be exact. To reflect EMI information of submodules, Liang et al. [11] and Sun et al. [12] built the models whose submodule output voltages are substituted by equivalent voltage sources. Considering the effects of stray parameters, control periods, power levels, etc., Zhu et al. [5] proposed a GPU-based parallel algorithm to calculate the EMI of MMC. Chen et al. [13] concluded that the submodules closer to ac output end are more sensitive to high d*v*/d*t* conditons, and Sun and Pei [14] verified that nearest level modulation (NLM) is doing better than phase-shifting carrier pulsewidth modulation (PSC-PWM) in EMI performance. In the aspect of conducted EMI reduction measures, several modulation-based methods to reduce CM voltage of output middle point are proposed in [15], [16], [17], [18], and [19]. The above references are summarized in Table I. More MMC EMI related references are summarized in [20].

TABLE I
EXISTING REFERENCES RELATED TO THE CONDUCTED EMI PROBLEMS OF MMC

Type	Ref.	Research object	Description	Evaluation
EMI modeling & analysis	[7]	Auxiliary power supply CM emission	CM EMI propagating path analysis	**Contributions:** The EMI models of bridge-arms and the whole converter are established in detail. **Drawbacks:** The EMI mechanisms are not revealed thoroughly, especially the way how EMI propagates inside and among submodules.
	[8]	Bridge-arm output voltage	Staircase-wave-based EMI source substitution	
	[9], [10]	Converter CM emission	Superposition theorem based model simplification	
	[11]	Submodule output/floating voltage	Superposition theorem based CM voltage analysis	
	[12]		Time-sequence-based EMI source modeling	
	[13]		Considering submodule switching states	
	[14]	Bridge-arm output voltage	EMI comparison of NLM and PSC-PWM	
EMI reduction	[15]	Converter AC neutral point voltage	Modulation-based spectrum spread	The modulation-based methods are more focused, while the stray parameter based methods are less studied.
	[16], [17]		Modulation-based CM voltage elimination	
	[18], [19]		Space position based spectrum spread	

Although former researches have done many works, the in-depth mechanisms of conducted EMI in MMC are still not revealed clearly. To overcome the drawbacks of previous articles, this article makes the following efforts. First, the circuit structure and modulation strategies of MMC are briefly introduced in Section II. Then, the submodule EMI models considering submodule switching states are built in Section III. In Section IV, the complete conducted EMI model of MMC is established, and the EMI propagating paths when submodules switch ON and switch OFF are analyzed. In Section V, the effects of submodule heatsink connecting patterns on EMI are discussed, and the mixed-mode (MM) EMI phenomenon appears when submodule heatsinks are all grounded. The simulation and experimental verification for EMI mechanisms and the MM EMI phenomenon are accomplished in Section VI. Finally, this article ends with conclusions and references.

II. MAIN CIRCUIT AND MODULATION METHODS OF MMC

A. Main Circuit of MMC

The main circuit of three-phase MMC is shown in Fig. 1. Each phase contains two bridge-arms, which are called the upper or positive bridge-arm (expressed by symbol p) and the lower or negative bridge-arm (expressed by symbol n). Each bridge-arm is in series of N submodules and one bridge-arm inductor. The submodules play the roles of supporting output voltages, while the bridge-arm inductors are fitted to suppress the circulating currents and smooth the output voltages. The middle points of three phases are connected to the ac side, such as grids, motors, loads, and filters. By controlling the number of ON-state submodules in one bridge-arm, different output voltages can be obtained on the ac side. Generally speaking, the number of ON-state submodules in one phase is kept to be constant N to avoid large circulating currents.

There are mainly two kinds of submodules for MMC: half-bridge submodule (HBSM) and full-bridge submodule (FBSM). For an HBSM, its output voltage can be 0 or U_C (the average voltage of submodule capacitors), while for an FBSM the output voltage can be 0, $+U_C$, or -U_C. The switching states of these two kinds of submodules and their corresponding output voltages are listed in Table II. The practical output voltages of other cases depend on the directions of submodule currents. Compared with HBSM, FBSM can output three kinds of voltage levels, which can enhance the flexibility of control algorithms and the ability of dc fault ride-through. However, the number of switching devices

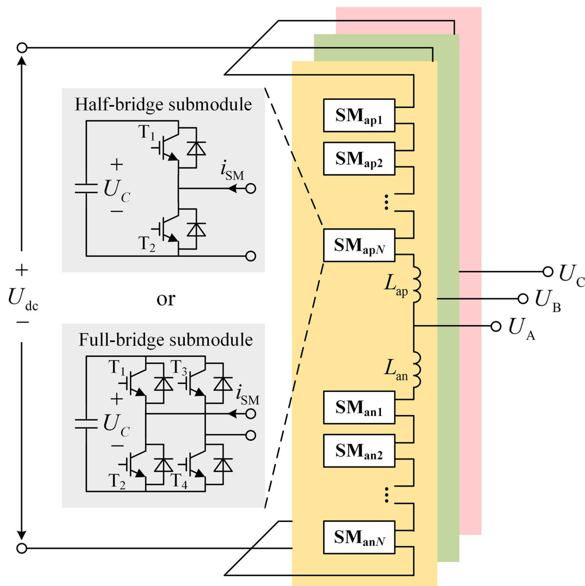

Fig. 1. Main circuit of a three-phase MMC.

TABLE II
SUBMODULE SWITCHING STATES AND OUTPUT VOLTAGES

Type	Output Voltage		
HBSM	T_1 ON and T_2 OFF (ON-state)	T_1 OFF and T_2 ON (OFF-state)	Other Cases (locked-state)
	U_C	0	U_C or 0
FBSM	T_1 ON and T_2 OFF T_3 OFF and T_4 ON (ON-state)	T_1 OFF and T_2 ON T_3 OFF and T_4 ON (OFF-state)	Other cases (locked-state or reversed on-state)
	U_C	0	U_C, $-U_C$, or 0

of the FBSM is twice of HBSM. Hence, a tradeoff between the output power quality and manufacturing cost should be carefully considered.

B. Modulation Methods of MMC

There are many kinds of modulation methods for MMC, such as NLM, PSC–PWM, and phase disposition modulation [2], [3]. As for NLM, the switching sequences are disarranged by the capacitor voltage sorting algorithm and it is difficult to predict the switching sequences. This brings great difficulties to the EMI mechanism research of MMC. Compared to NLM, PSC–PWM has two advantages. First, the switching pulse sequences of PSC–PWM are regular and easy to be predicted. Second, the capacitor voltages can be balanced automatically under open-loop control without breaking the regularities of switching sequences. Considering that the major concern of this article is the EMI mechanism during switching processes rather than the prediction of switching sequences, the selection of modulation methods makes no difference. For the convenience of later analysis in this article, only PSC–PWM is briefly introduced here. The basic operation principles of PSC–PWM are as follows:

1) Carriers: Each submodule has its own carrier. For a bridge-arm with N submodules, there are N different carriers, with the carrier phase offset of two adjacent submodules being $2\pi/N$. If the initial carrier phase of the first submodule is Φ, then the initial phases of the followings would be $\Phi+2\pi/N$, $\Phi+2\times2\pi/N$, …, $\Phi+(N-1)\times2\pi/N$.
2) Modulated waves: For each phase, the sine modulated waves of the upper and the lower bridge-arm have the same amplitude and frequency but reverse phases. While for three phases, the sine modulated waves of the bridge-arms on the same side differ 120° from each other.

III. EMI Models of Submodules Considering Submodule Switching States

To have an insight into the EMI mechanisms of MMC, an accurate EMI model should be built at first. Thereinto, the EMI modeling for submodules is one of the most critical steps. This is because that the submodules act as either EMI sources or paths, depending on the submodule switching states.

The high-frequency EMI models of ON-state and OFF-state submodules are shown in Fig. 2(a) and 2(b), respectively. For the HBSM, it is composed of one capacitor and two semiconductor switches, where ESR and ESL are the parasitic resistance and parasitic inductance of submodule capacitor. The semiconductor switches are mounted on the heatsinks, forming three important kinds of stray capacitance: C_C, C_O, and C_E, which stand for collector-heatsink capacitance, output-heatsink capacitance, and emitter-heatsink capacitance, respectively. The stray capacitance is important propagating paths of ground currents. When a submodule is working at ON-state, C_O is linked to the positive of capacitor; when the submodule is working at OFF-state, C_O is linked to the negative.

In fact, the high-frequency models of semiconductor switch are much more complicated [21], [22], [23], but it does not

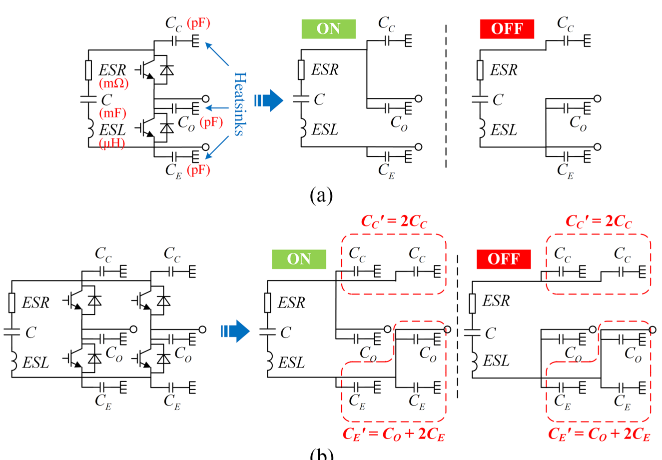

Fig. 2. EMI models of (a) HBSM and (b) FBSM.

influence the path analysis in this article. This is because that although there is nH-level lead inductance and pF-level diode junction capacitance, the noise directions are barely affected. For the convenience of path analysis, this article regards ON-state as short-circuit and OFF-state as open-circuit, regardless of the complicated effects such as the fast recovery of diode.

For an FBSM working at half-bridge mode, it has similar models with the HBSM. This is because the stray capacitance in the upper red dotted box can be seen as a whole where

$$C_{C'} = 2C_C. \tag{1}$$

The stray capacitance in lower red dotted box can also be seen as a whole where

$$C_{E'} = C_O + 2C_E. \tag{2}$$

For the convenience of following analysis, only HBSM is studied in the rest part of this article, and "submodule" refers to "HBSM" unless particularly stated.

Except for the aforementioned two kinds of static states (ON-state and OFF-state), there are another two dynamic states: switching-ON state and switching-OFF state. The difference of dynamic-state and static-state submodules is that there is a voltage source in a dynamic-state submodule. The capacitor voltage is not constant because there are dc, fundamental, and second harmonic components. Different switching time has different capacitor voltage magnitude. Hence, the amplitude of the voltage source u_C is the instantaneous voltage value of submodule capacitor when the switching behavior occurs.

The four kinds of submodule switching states and their EMI models are shown in Table III. Different from previous models that replace the whole submodule by a voltage source, the proposed method put the equivalent voltage sources inside submodules to reveal how EMI propagates in submodules.

The EMI model of a submodule is not fixed because the switching state changes with time. For a specific submodule, it may act as an EMI source at some switching moment, and part of EMI propagating paths at another moment. That is to

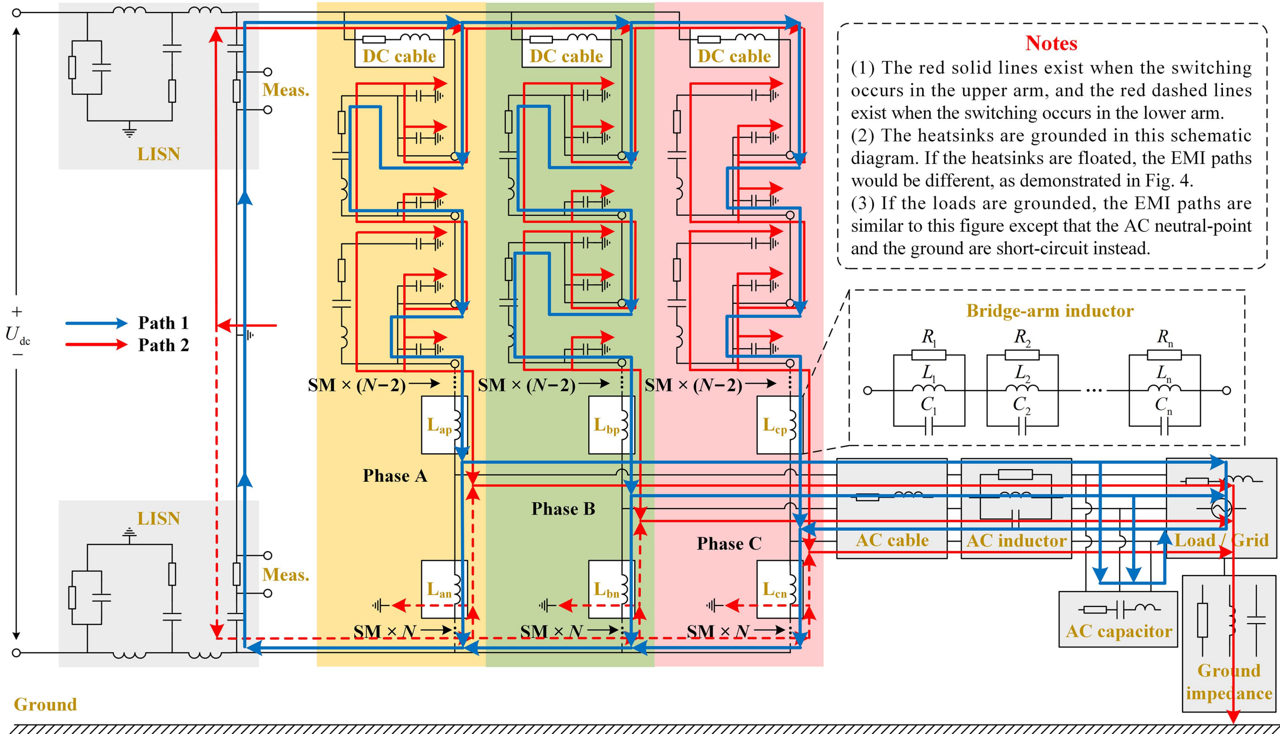

Fig. 3. Complete conducted EMI model of three-phase MMC.

TABLE III
SUBMODULE EMI MODELS OF DIFFERENT SWITCHING STATES

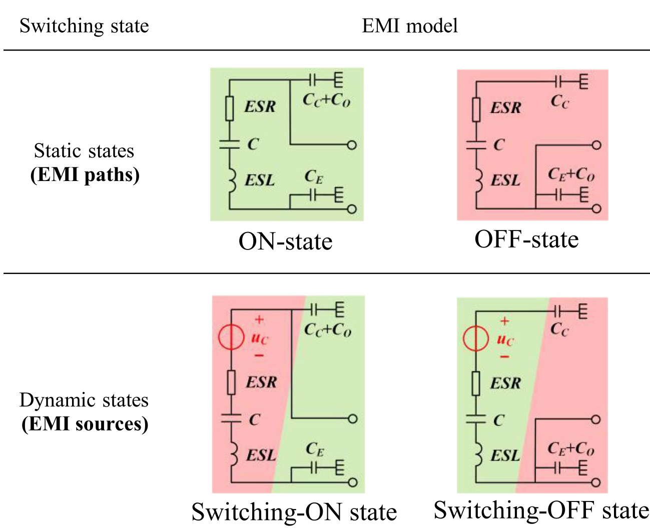

Switching state	EMI model	
Static states **(EMI paths)**	ON-state	OFF-state
Dynamic states **(EMI sources)**	Switching-ON state	Switching-OFF state

Notes: According to the direction of input current, there are actually four dynamic states (switching on/off with positive/negative input current). The semiconductor switch and its anti-parallel diode are seen as a short-circuit or open-circuit whole for the convenience of EMI path analysis in this paper.

say, the submodule EMI model is changing with its switching state. After the submodules EMI models being established, the complete EMI model of MMC can then be obtained, which will be introduced in the next section.

IV. Complete EMI Model of MMC Based on Submodule Switching-On and Switching-Off Processes

The complete conducted EMI model of a three-phase MMC is demonstrated in Fig. 3. The passive elements (such as bridge-arm inductors, dc and ac cables, ac filters, etc.) are important components of EMI propagating paths, but the high-frequency models are simplified for the convenience of image drawing. The LISNs are added to isolate the EMI from dc side and provide standardized measuring ports of EMI.

In traditional EMI analysis methods, the EMI propagating paths are divided into CM and DM paths, and the total EMI is the sum of CM EMI and DM EMI [24]. The EMI flowing among phase lines and the ground is usually thought be to CM EMI, while the EMI flowing between two phases is thought to be DM EMI. However, this method is not applicable for EMI analysis of MMC. This is because that CM EMI and DM EMI are not well decoupled in MMC, which will be explained in Section V. Similar to traditional classification, the EMI paths are divided into the following two kinds, according to whether the noise current goes through the heatsink/ground:

Path 1. The main circuit: As is illustrated by the blue arrows in Fig. 3, the noise distribution in this path is similar to harmonic-frequency (about several kHz) currents except that the concerned EMI noise belongs to higher frequency band (far more than several kHz). According to the superposition theorem that components with different frequencies do not interplay with each other, the harmonic currents (such as second circulating current) have few effects on high-frequency EMI. When a submodule works at ON-state, the main circuit noise goes through

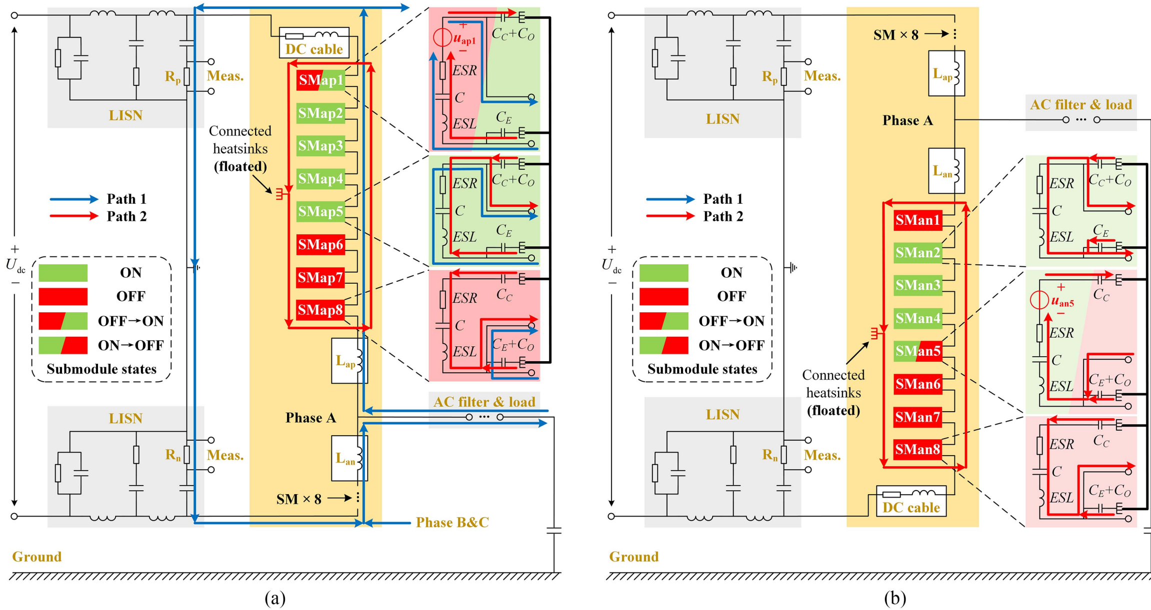

Fig. 4. EMI models during submodule switching processes: (a) switching-ON process in upper bridge-arm and (b) switching-OFF process in lower bridge-arm.

the capacitor. When a submodule works at OFF-state, the main circuit noise goes through the lower switch.

Path 2. The heatsink/ground: As is illustrated by the red arrows in Fig. 3, the noise current in this path goes through C_C, C_O, and C_E. If the heatsinks are grounded, the noise current flows into the ground directly. If the heatsinks are floated, the noise current circulates inside submodule itself or flows into other submodules, depending on the connecting patterns of heatsinks. The detailed effects of heatsink connecting patterns on EMI are discussed in Section V.

To describe the EMI mechanisms of MMC, two typical cases are emphatically discussed: submodule switching-ON process and switching-OFF process. Considering that the three-phase case is similar to single-phase, only Phase A is studied here. It is assumed that there is only one switching-ON state submodule SM_{ap1} in the upper bridge-arm, and only one switching-OFF state submodule SM_{an5} in the lower bridge-arm.

Actually, Phase B and Phase C have some effects on the EMI paths of Phase A as well. The noise current excited by the EMI sources in Phase A can also flow into Phase B and Phase C because the three phases are in parallel in circuit structure. However, compared to the impedance of the measuring ports of LISNs (about 100 Ω), the path impedance of Phase B and Phase C is far greater because there are two bulky bridge-arm inductors in each phase. Hence, the noise current mainly goes through the LISNs on the dc side.

A. EMI Model for Submodule Switching-on Process

The EMI model of submodule switching-ON process is shown in Fig. 4(a). For the sake of keeping consistent with the simulation and experimental verification in Section VI, N is set to be 8 here. SM_{ap1} is at switching-ON state, while other submodules are at static states. Obviously, SM_{ap1} acts as the EMI source at

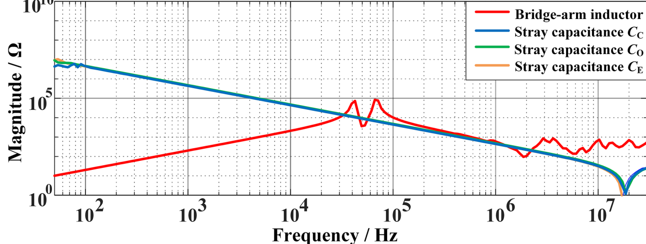

Fig. 5. Magnitude-frequency diagram of impedance.

the present switching moment, while other submodules are part of the EMI propagating paths. The noise currents generated by the step voltage source of SM_{ap1} goes through both Path 1 and Path 2. When other submodules switch, SM_{ap1} becomes part of the EMI propagating paths and SM_{ap1} is not an EMI source anymore.

The bridge-arm inductors are natural EMI filters because the order of magnitudes of inductance is mH in general. The great impedance can suppress the amplitudes of noise currents and avoid the EMI from spreading to the other bridge-arm. The magnitude-frequency diagram of the bridge-arm inductor impedance and the stray capacitance impedance is figured in Fig. 5. In low-frequency band, the noise current in Path 1 takes the domination because the impedance of bridge-arm inductor is not too high and the noise current in Path 2 is low in magnitude. While in high-frequency band, the filtering function of bridge-arm inductors begins to strengthen and the isolation function of stray capacitance begins to weaken. That is to say, the noise current in Path 2 dominates as frequency increases. If the heatsinks are connected together but not grounded, the noise current in Path 2 would circulate inside the bridge-arm that the dynamic-state submodule lies in.

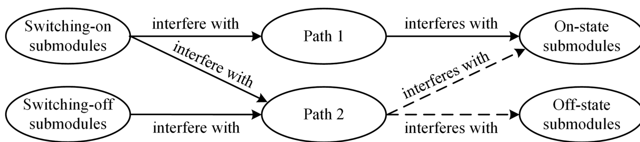

Fig. 6. Relations of switching states and EMI propagating paths.

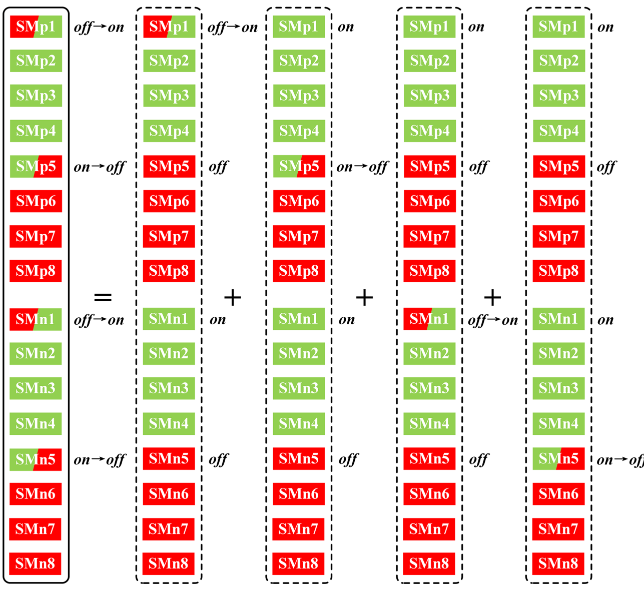

Fig. 7. Equivalent EMI model for multiple dynamic state submodules.

B. EMI Model for Submodule Switching-off Process

The EMI model of submodule switching-OFF process is illustrated in Fig. 4(b). SM_{an5} is at switching-OFF state and other submodules are at static states. Obviously, SM_{an5} acts as the EMI source at the present switching moment, while other submodules act as EMI propagating paths. Different from the switching-ON process, the noise currents generated by the step voltage source of SM_{an5} only goes through Path 2 because the step voltage source is not in series with Path 1. When other submodules switch, SM_{an5} becomes part of EMI propagating paths and SM_{an5} is not the EMI source anymore.

In Fig. 4(b), the noise current comes from the positive of the step voltage source and goes into the heatsink/ground through the C_C of SM_{an5}, then comes back from the stray capacitance of other submodules and the cables that connect different submodules. Similar to the switching-ON process, the noise current would not flow into the other bridge-arm due to the large impedance of bridge-arm inductors. To visually describe the complicated relations of switching states and EMI propagating paths, a logical diagram is drawn in Fig. 6. The dashed arrows exist only when different submodule heatsinks are connected together.

If there are more dynamic-state submodules at a switching moment, the proposed models are still applicable by simply applying the superposition theorem. As is shown in Fig. 7, SM_{p1} and SM_{n1} are at switching-ON state, while SM_{p5} and SM_{n5} are at switching-OFF state. By using the superposition theorem, the total model is the superposition of four submodels. In each submodel, there is only one dynamic-state submodule, and the EMI propagating mechanisms are the same with the former analysis.

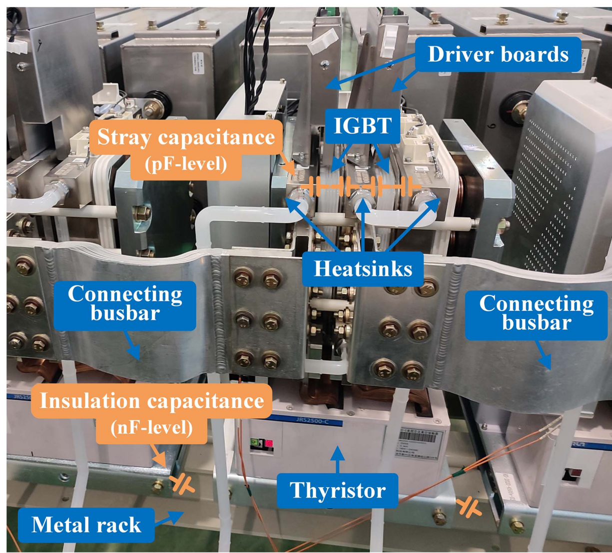

Fig. 8. Submodule prototype in practical engineering.

According to the analysis, four important characteristics of the EMI performance of MMC can be summarized as follows:

1) The EMI in Path 1 is greatly suppressed by the bridge-arm inductors, so the EMI in Path 2 can barely flow into the other bridge-arm.
2) The EMI in Path 1 is only excited by switching-ON state submodules, while the EMI in Path 2 is excited by both switching-ON state and switching-OFF state submodules.
3) The ON-state submodules are affected by two paths, while the OFF-state submodules are only affected by Path 2.
4) When the heatsinks are separated and floated, the EMI in Path 2 only circulates in switching-state submodules, and no EMI can be detected in OFF-state submodules.

V. Mixed-Mode EMI Phenomenon in MMC

This section introduces the effect of submodule heatsink connecting patterns on EMI, which has been mentioned in Section IV. The MM EMI phenomenon based on grounded submodule heatsinks is also explained in this part.

A. Effects of Submodule Heatsink Connecting Patterns

As is demonstrated in Fig. 8, the submodule heatsinks are usually mounted on the metal racks by bolts in practical engineering. The metal racks are painted by insulating coating to avoid from rusting. In low-frequency band (below MHz), the insulation layer plays a good role of electric isolation, so the heatsinks can be seen as floated to the metal racks. While in high-frequency band (above MHz), the impedance of equivalent insulation capacitance (nF-level) begins to decrease, and the heatsinks can be approximately seen as connected to the racks.

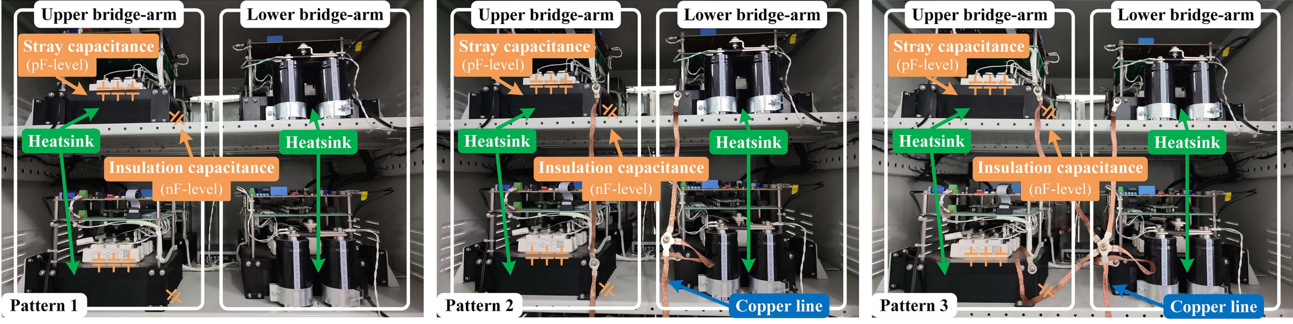

Fig. 9. Three kinds of heatsink connecting patterns: (a) submodule-floated (Pattern 1); (b) bridge-arm-floated (Pattern 2); and (c) phase-floated (Pattern 3).

In general, the heatsinks of different submodules are mounted on the same racks to decrease the bridge-arm volume, which leads to potential EMI paths among submodules.

To study the effects on EMI, three kinds of connecting patterns are discussed here. Fig. 9 shows how the submodule heatsinks are connected in a prototype MMC. The copper lines are used to ensure good connections of submodule heatsinks. It is noted that although the heat-dissipating method in Fig. 9 is different from Fig. 8, the basic EMI paths are similar.

Pattern 1. Submodule-floated: The submodule heatsinks are neither connected together nor grounded. There are more than $2N$ isolated heatsinks in one phase, and EMI only flows in Path 1. The noise currents in different submodule heatsinks will not affect each other.

Pattern 2. Bridge-arm-floated: The submodule heatsinks in the same bridge-arm are connected but not grounded. There are two submodule heatsink systems in one phase: the upper heatsink system and the lower heatsink system. These two submodule heatsink systems are separated to each other. The noise currents in heatsinks only circulate inside the bridge-arm.

Pattern 3. Phase-floated: The submodule heatsinks in the same phase are connected but not grounded. Because of the filtering and isolation functions of bridge-arm inductors, the submodule heatsink system can be still divided into two separated parts: the upper and the lower bridge-arms. The EMI paths of Pattern 3 are similar to Pattern 2 in high frequency.

The submodule heatsink connecting patterns mainly affect the path impedance of Path 2, which is the impedance between the positive and negative of the step voltage source. Generally speaking, high isolation degree of heatsinks means high heatsink path impedance and low EMI amplitude in Path 2. Obviously, Pattern 1 is doing better than Pattern 2 and 3 in EMI performance. However, higher insulation degree means larger submodule volumes and higher insulation costs.

Equations (3)–(8) show the path impedance of the above three connecting patterns. In these equations, j is the imaginary unit, ω is the angular frequency of signals, m is the number of adjacent OFF-state submodules above dynamic-state submodule, and n is the number of adjacent OFF-state submodules below dynamic-state submodule. For example, as is shown in Fig. 4, m and n both equal to 0 for $\mathrm{SM_{ap1}}$, while m equals to 0 and n equals to 3 for $\mathrm{SM_{an5}}$. The path impedance values of Pattern 2 and 3 are related to m and n. The bigger m and n are, the smaller the path impedance will be. By analyzing the items of (3)–(8), it can be seen that their first items are the same but other items are different. Obviously, the impedance of Pattern 1 is bigger than Pattern 2 and 3 because $m \geq 0$ and $n \geq 0$. The derivation procedures of following equations are given in Appendix:

$$Z^{\mathrm{Pattern_1}}_{\mathrm{Switching-on}} = \left(\frac{1}{j\omega C} + ESR + j\omega\cdot ESL\right) + \frac{1}{j\omega\left[(C_C+C_O)//C_E\right]} \tag{3}$$

$$Z^{\mathrm{Pattern_1}}_{\mathrm{Switching-off}} = \left(\frac{1}{j\omega C} + ESR + j\omega\cdot ESL\right) + \frac{1}{j\omega\left[C_C//\left(C_O+C_E\right)\right]} \tag{4}$$

$$Z^{\mathrm{Pattern_2}}_{\mathrm{Switching-on}} \approx \left(\frac{1}{j\omega C} + ESR + j\omega\cdot ESL\right) + \frac{1}{j\omega\left[(m+1)\left(C_E+C_O\right)+C_C\right]} + \frac{1}{j\omega\left[(n+1)\left(C_E+C_O\right)+C_C\right]} \tag{5}$$

$$Z^{\mathrm{Pattern_2}}_{\mathrm{Switching-off}} \approx \left(\frac{1}{j\omega C} + ESR + j\omega\cdot ESL\right) + \frac{1}{j\omega C_C} + \frac{1}{j\omega\left[(m+n+2)\left(C_E+C_O\right)+C_C\right]} \tag{6}$$

$$Z^{\mathrm{Pattern_3}}_{\mathrm{Switching-on}} \approx Z^{\mathrm{Pattern_2}}_{\mathrm{Switching-on}} \tag{7}$$

$$Z^{\mathrm{Pattern_3}}_{\mathrm{Switching-off}} \approx Z^{\mathrm{Pattern_2}}_{\mathrm{Switching-off}}. \tag{8}$$

B. Mixed-Mode EMI Phenomenon

The MM EMI phenomenon is first discovered by Zhang et al. [25]. This phenomenon reveals that CM and DM EMI are coupled when the converter is asymmetric. That is to say, CM EMI and DM EMI can transform into each other. This phenomenon also appears in MMC. On some low-voltage occasions, the submodule heatsinks of MMC are directly connected to the ground. Under this circumstance, the MM EMI phenomenon can be observed.

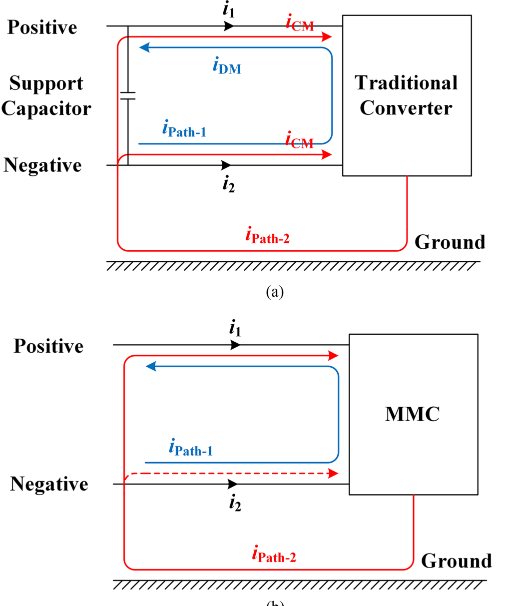

Fig. 10. Relations of dc currents and i_{CM}, i_{DM} in (a) traditional converter and (b) MMC.

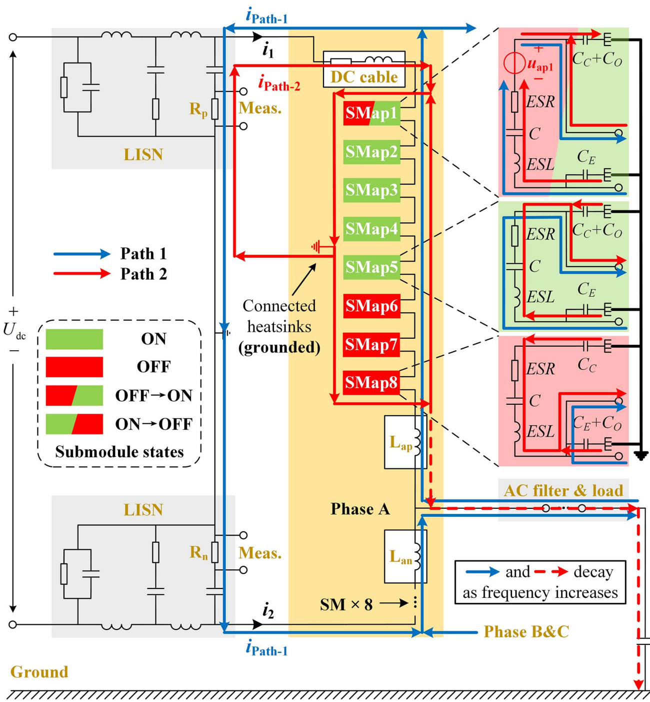

Fig. 11. Detailed EMI paths under mixed-mode EMI phenomenon.

As is illustrated in Fig. 10(a), according to the traditional CM/DM theory, the CM current is defined as

$$i_{\mathrm{CM}} = \frac{i_1 + i_2}{2} = \frac{i_{\mathrm{Path-2}}}{2} \tag{9}$$

and the DM current is defined as

$$i_{\mathrm{DM}} = \frac{i_1 - i_2}{2} = -i_{\mathrm{Path-1}} \tag{10}$$

where i_1 is the dc positive current and i_2 is the dc negative current. In traditional opinions, i_{CM} is thought to be equal to half of $i_{\mathrm{Path-2}}$, the ground current, and it is evenly distributed in power lines. While i_{DM} is thought to be equal to $i_{\mathrm{Path-1}}$ in amplitude, the noise current is in main circuit. When the circuit is symmetric, i_{CM} is independent of i_{DM}.

However, the traditional CM/DM theory cannot explain the EMI mechanisms and the MM EMI phenomenon in MMC. As is shown in Fig. 10(b), $i_{\mathrm{Path-1}}$ goes across the dc side like traditional i_{DM}, while $i_{\mathrm{Path-2}}$ only goes through one of the dc power lines rather than two lines at one time. Under this circumstance, $i_{\mathrm{Path-2}}$ generates both CM and DM components. The total DM current is the sum of $i_{\mathrm{Path-1}}$ and the DM component generated by $i_{\mathrm{Path-2}}$. That is to say, the CM and DM EMI in MMC are coupled. The EMI paths of MMC under MM EMI phenomenon are as demonstrated in Fig. 11.

According to the definitions of CM and DM currents, the CM current of MM phenomenon is

$$\begin{aligned} i_{\mathrm{CM'}} &= \frac{i_1 + i_2}{2} = \frac{(i_{\mathrm{Path-2}} - i_{\mathrm{Path-1}}) + i_{\mathrm{Path-1}}}{2} \\ &= \frac{i_{\mathrm{Path-2}}}{2} = i_{\mathrm{CM}}. \end{aligned} \tag{11}$$

And the DM current comes from two parts: one from $i_{\mathrm{Path-2}}$ while the other one from $i_{\mathrm{Path-1}}$

$$\begin{aligned} i_{\mathrm{DM'}} &= \frac{i_1 - i_2}{2} = \frac{(i_{\mathrm{Path-2}} - i_{\mathrm{Path-1}}) - i_{\mathrm{Path-1}}}{2} \\ &= \frac{i_{\mathrm{Path-2}}}{2} - i_{\mathrm{Path-1}}. \end{aligned} \tag{12}$$

Substituting (11) into (12)

$$i_{\mathrm{DM'}} = i_{\mathrm{CM'}} - i_{\mathrm{Path-1}}. \tag{13}$$

Equation (11) shows that the CM current does not change even if the EMI paths are not symmetric, while (13) shows that CM and DM currents on dc side are dependent to each other and there is additional DM component. In low-frequency band, $i_{\mathrm{Path-1}}$ is far greater than $i_{\mathrm{Path-2}}$. As frequency increases, the bridge-arm inductor impedance becomes larger and the stray capacitance impedance gets smaller. $i_{\mathrm{Path-1}}$ decays to zero and $i_{\mathrm{Path-2}}$ dominates. Under this circumstance, the DM component only comes from $i_{\mathrm{Path-2}}$ and CM current equals to DM current.

The appearance of MM EMI phenomenon in MMC is caused by the following four critical factors:

1) The grounded submodule heatsinks provide the EMI propagating paths for the ground current in Path 2.
2) Because of the isolation function of bridge-arm inductors, the noise current in Path 2 is trapped inside the bridge-arm that the dynamic-state submodule lies in.
3) There is no dc support capacitor to provide a short-circuit path for the noise current in Path 2. The current is not evenly distributed in positive and negative lines.

TABLE IV
SIMULATION PARAMETERS FOR THREE-PHASE MMC

Parameters	Symbol	Value
DC voltage	U_{dc}	200V
AC output phase voltage (peak value)	U_{ac}	90V
Capacitor average voltage	U_C	22–23V
Modulation ratio	M	0.9
Number of bridge-arm submodules	N	8
Frequency of carrier waves	f_c	1kHz
Adopted modulation strategy	PSC-PWM	
Adopted voltage-balancing Method	Self-balance (open-loop control)	

4) Sometimes the switching actions of upper and lower bridge-arms may not appear in pairs, which create an asymmetric working condition.

The MM phenomenon revealed that traditional CM/DM based EMI analysis method is not applicable for all converters. The coupled component of CM and DM EMI is often overlooked in traditional analysis method, which would cause undesired errors to EMI prediction and reduction when the converter is not perfectly symmetric.

VI. SIMULATION AND EXPERIMENTAL VERIFICATION

A. Simulation Verification

To verify the EMI mechanisms as well as the existence of MM EMI phenomenon, a simulation model of MMC is built in ANSYS Simplorer. The simulation parameters are list in Table IV. Fig. 12 shows the switching sequences of Phase A, and 0.8 ms is chosen for observation. The capacitor voltages of six representative submodules are shown in Fig. 13.

When the heatsinks are submodule-floated (Patter 1), the voltage oscillations only appear in dynamic-state submodules. When the heatsinks are bridge-arm floated (Pattern 2), the voltage oscillations also appear in static-state submodules. The cases under Pattern 3 are similar to Pattern 2 except some differences of oscillation amplitudes. These results prove that the ON-state submodules are affected by two paths, while the OFF-state submodules are only affected by Path 2.

As for the MM EMI phenomenon, it can be seen from Fig. 14 that the CM component is smaller than the DM component below 20 kHz, while they are equal above 20 kHz. This is because that the CM and DM components are both generated by $i_{\text{Path-2}}$ in high-frequency band, while $i_{\text{Path-1}}$ contributes almost no DM component. This result proves the accuracy of Characteristic 1 in Section IV that the noise current of Path 2 can barely flow into the other bridge-arm.

B. Experimental Verification

To verify the proposed EMI mechanisms of MMC, some experiments are conducted in a laboratory-level three-phase MMC prototype. The experiment layout is shown in Fig. 15.

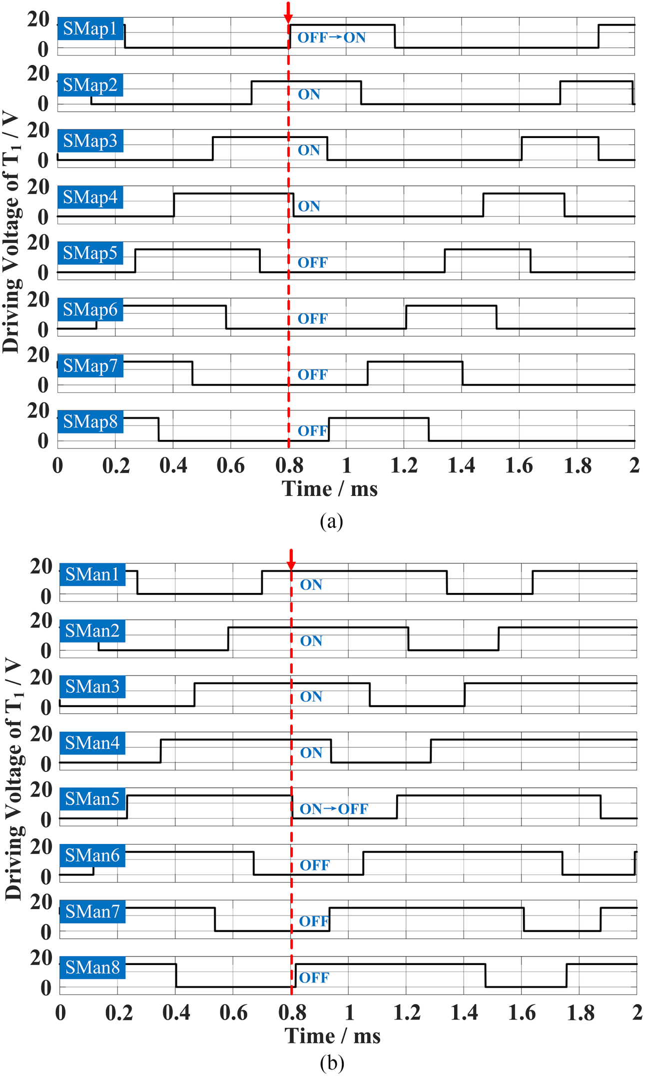

Fig. 12. Switching sequences: (a) upper arm and (b) lower arm.

The connecting patterns of submodule heatsinks are shown in Fig. 9. The basic experiment parameters are the same with the simulation parameters in Table IV except that the modulation ratios of upper and lower bridge-arms are different.

For the convenience of experimental verification, the modulation ratios of upper and lower bridge-arms are set to be different constants. In these experiments, M_p (the modulation ratio of upper bridge-arm) is 0.75 and M_n (the modulation ratio of lower bridge-arm) is 0.25. This method can ensure that the upper and lower bridge-arms do not switch at the same time, so the effect of the other bridge-arm can be excluded. Besides, constant modulation ratios can keep the balance of capacitor voltages inside bridge-arms. The capacitor voltages of three representative submodules are demonstrated in Fig. 16, where $\text{SM}_{\text{ap}x}$ represents dynamic-state submodule in the upper bridge-arm, and $\text{SM}_{\text{ap}y}$ and $\text{SM}_{\text{an}z}$ represent other submodules in upper and lower bridge-arms.

According to the experiment results in Fig. 16, when the heatsinks are submodule-floated (Pattern 1), there are only two

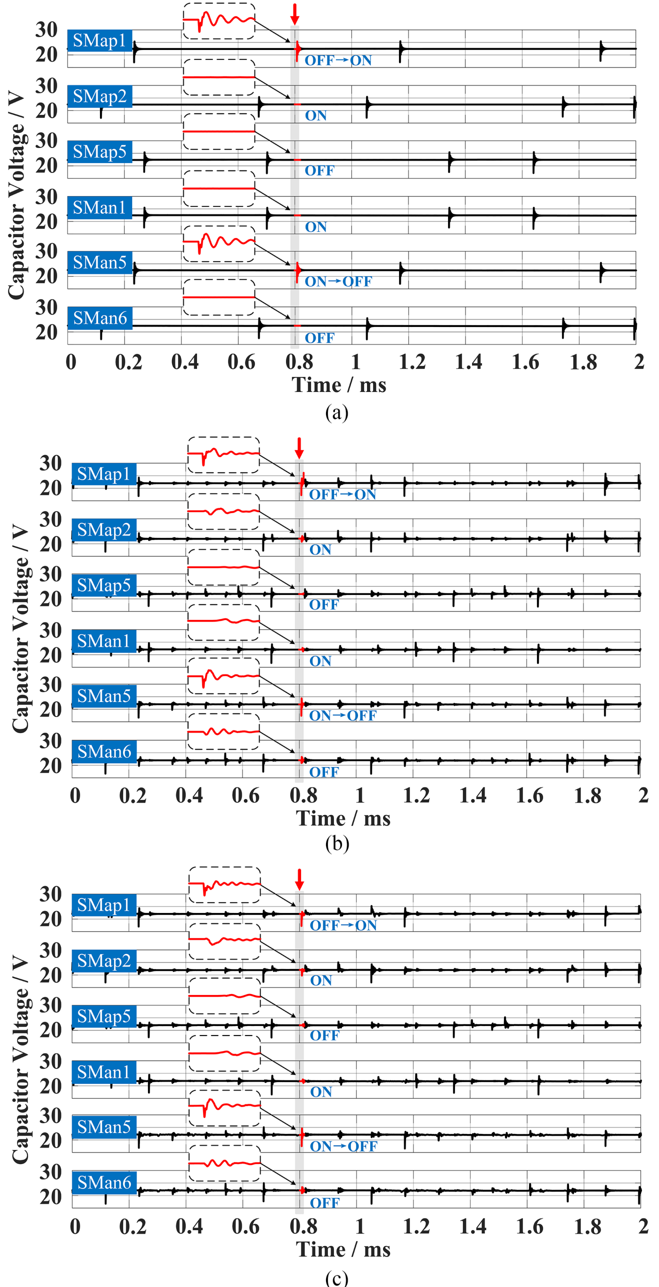

Fig. 13. Capacitor voltages of representative submodules (simulation): (a) Pattern 1; (b) Pattern 2; and (c) Pattern 3.

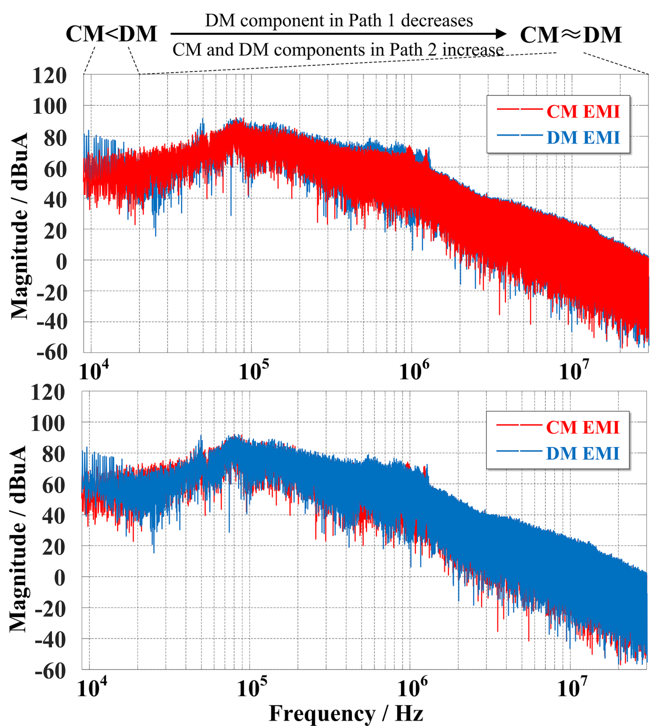

Fig. 14. Simulation spectra of CM and DM currents on dc side.

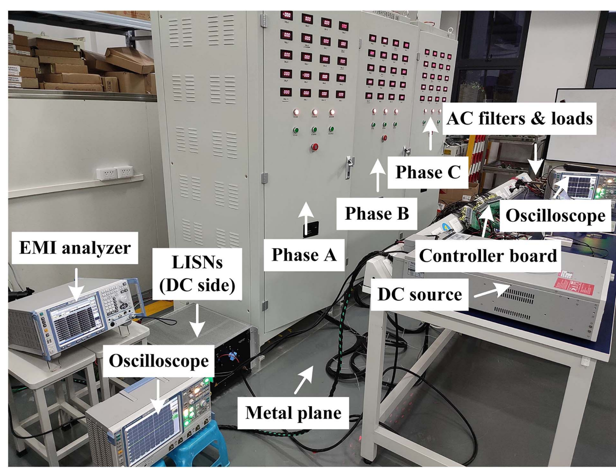

Fig. 15. Experiment layout.

voltage oscillations in one switching period for a submodule. The voltage oscillations are caused by the switching actions of the submodule itself rather than other submodules. The voltage oscillations caused by switching actions are marked by red arrows. The switching moments of different submodules are inconsistent because the switching pulses are not the same.

When the heatsinks are bridge-arm-floated (Pattern 2) or phase-floated (Pattern 3), there are eight voltage oscillations for upper bridge-arm submodules, and two voltage oscillations for lower bridge-arm submodules. The number difference of oscillations is caused by different modulation ratios. The voltage oscillations of submodules in the same bridge-arm occur at the same time, while the case is different for lower bridge-arm submodules. This result proves the accuracy of Characteristic 1 in Section IV that EMI in Path 2 can barely flow into the other bridge-arm.

The spectra of CM and DM EMI on dc side are shown in Fig. 17. The spectra show that CM EMI is smaller than DM EMI below 10 kHz, and they approximately accord with each other above 10 kHz, which agrees with the aforementioned analysis. This result proves the accuracy of proposed EMI mechanisms and MM EMI phenomenon in MMC. It should be noted that even though there are some amplitude errors with the simulation

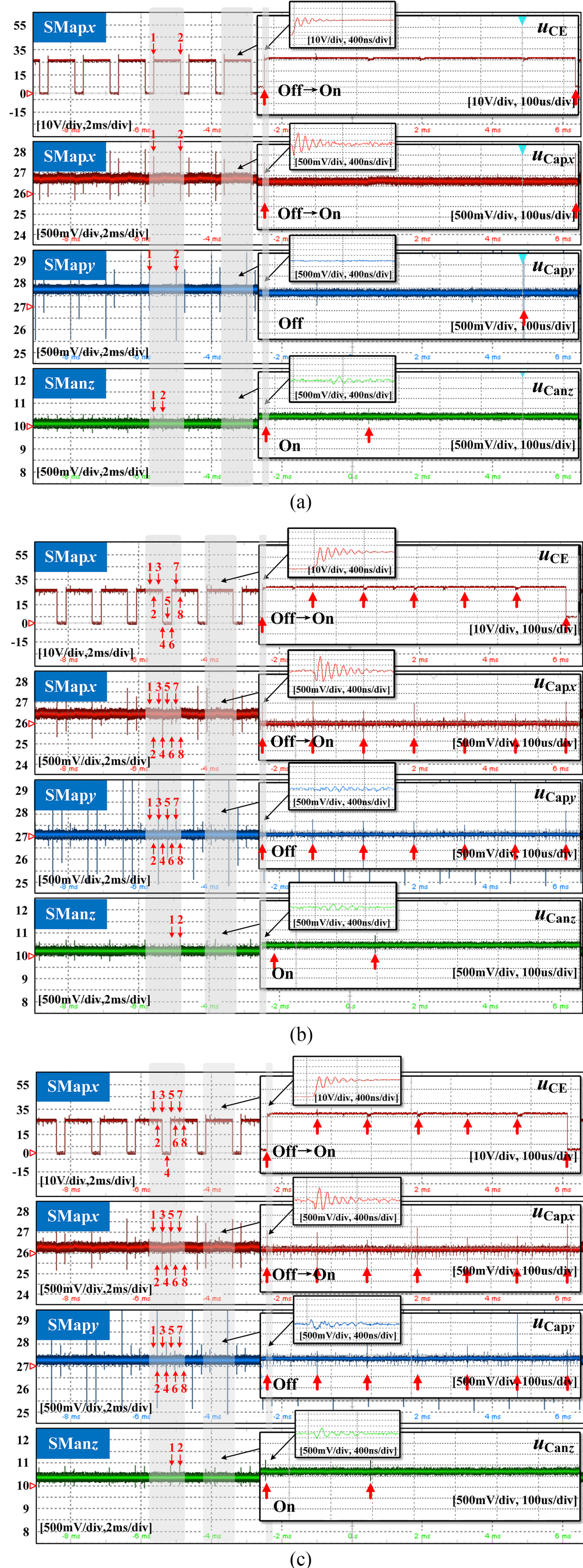

Fig. 16. Capacitor voltages of representative submodules (experiment, $M_p = 0.75$, $M_n = 0.25$): (a) Pattern 1; (b) Pattern 2; and (c) Pattern 3.

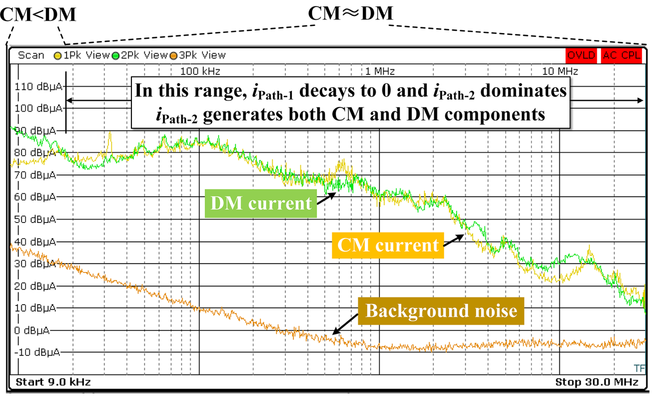

Fig. 17. Experiment spectra of CM and DM currents on dc side.

results in Fig.14, the shapes of spectra envelop are alike. The errors may be caused by the measuring and fitting errors of element impedance.

VII. Conclusion

In this article, an EMI model of MMC considering the switching states of submodules is built. Analysis shows that dynamic-state submodules are EMI sources in MMC and static-state submodules are parts of EMI propagating paths. Based on the established model, this article studies and verifies the detailed EMI mechanisms of MMC. Besides, the MM EMI phenomenon in MMC is discovered and explained.

The contributions made by this article are as follows:

1) A conducted EMI model of MMC is proposed. Different from previous models that replace the whole submodule by an equivalent voltage source and neglect the internal situations of submodules, the proposed model considers the submodule switching states. Besides, the way how EMI propagates inside submodules is analyzed.
2) Simulation and experiment results show that submodule heatsink connecting patterns have effects on EMI paths. High insulation degree of heatsinks means high heatsink path impedance and low EMI amplitude.
3) The MM EMI phenomenon in MMC is analyzed. When the converter is not symmetric in topology or switching mode, the CM and DM interference would be coupled. The coupled component is often overlooked in traditional CM/DM based EMI analysis method, causing undesired errors to EMI prediction and reduction.

Appendix

Figs.18 and 19 show the equivalent circuits for four kinds of switching states. For an ON-state submodule, its input impedance is C_C+C_O from the left and C_E from the right. For an OFF-state submodule, its input impedance is C_E+C_O from both sides. Equations (3)–(8) are derived as follows.

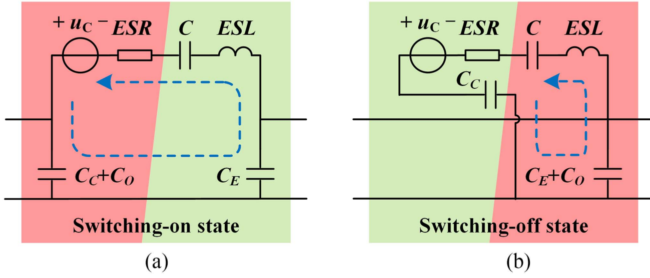

Fig. 18. Equivalent circuits for (a) switching-ON state submodule and (b) switching-OFF state submodule.

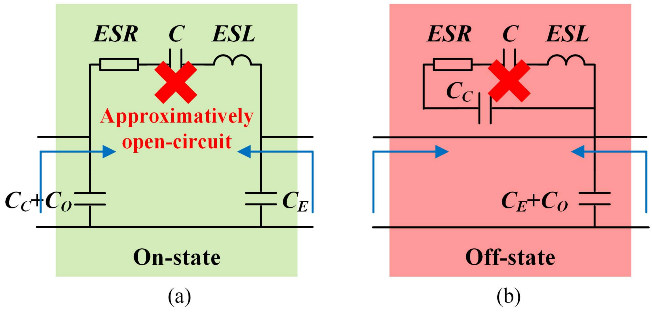

Fig. 19. Equivalent circuits for (a) ON-state submodule; and (b) OFF-state submodule.

A. Path Impedance of Switching-on Submodule (Pattern 1)

The switching-ON state submodule is separated to other submodules, so the path impedance is as shown in Fig. 18(a)

$$Z_{\text{Switching-on}}^{\text{Pattern_1}} = \left(\frac{1}{j\omega C} + ESR + j\omega \cdot ESL\right) + \frac{1}{j\omega\left[\left(C_C + C_O\right)//C_E\right]}. \quad \text{(A.1)}$$

B. Path Impedance of Switching-off Submodule (Pattern 1)

The switching-OFF state submodule is separated to other submodules, so the path impedance is as shown in Fig. 18(b)

$$Z_{\text{Switching-off}}^{\text{Pattern_1}} = \left(\frac{1}{j\omega C} + ESR + j\omega \cdot ESL\right) + \frac{1}{j\omega\left[C_C//\left(C_O + C_E\right)\right]}. \quad \text{(A.2)}$$

C. Path Impedance of Switching-on Submodule (Pattern 2)

The switching-ON state submodule is connected to other submodules. Fig. 20(a) shows the simplified equivalent circuit

$$Z_{\text{Switching-on}}^{\text{Pattern_2}} \approx \left(\frac{1}{j\omega C} + ESR + j\omega \cdot ESL\right) + \frac{1}{j\omega\left[(m+1)\left(C_E + C_O\right) + C_C\right]} + \frac{1}{j\omega\left[(n+1)\left(C_E + C_O\right) + C_C\right]}. \quad \text{(A.3)}$$

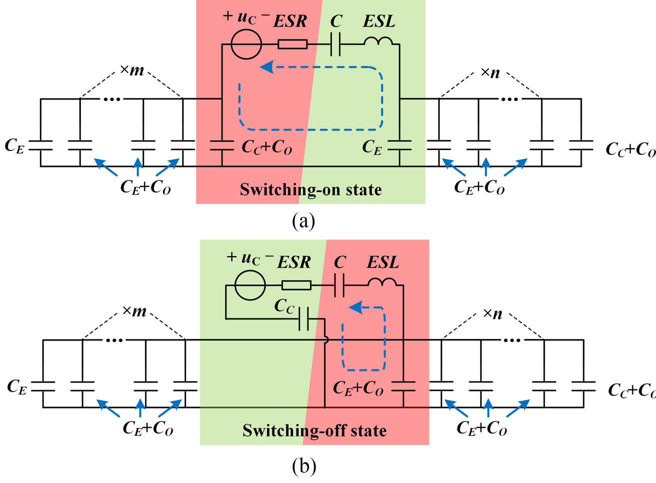

Fig. 20. Equivalent circuits under Pattern 2 and 3 for (a) switching-ON state submodule; and (b) switching-OFF state submodule.

D. Path Impedance of Switching-off Submodule (Pattern 2)

The switching-OFF state submodule is connected to other submodules. Fig. 20(b) shows the simplified equivalent circuit. The path impedance is

$$Z_{\text{Switching-off}}^{\text{Pattern_2}} \approx \left(\frac{1}{j\omega C} + ESR + j\omega \cdot ESL\right) + \frac{1}{j\omega C_C} + \frac{1}{j\omega\left[(m+n+2)\left(C_E + C_O\right) + C_C\right]}. \quad \text{(A.4)}$$

E. Path Impedance of Switching-on Submodule (Pattern 3)

Because of the high impedance of bridge-arm inductors, the bridge-arms are divided into two separate parts. Thus, the equivalent circuit is similar to Fig. 20(a), and

$$Z_{\text{Switching-on}}^{\text{Pattern_3}} \approx Z_{\text{Switching-on}}^{\text{Pattern_2}}. \quad \text{(A.5)}$$

F. Path Impedance of Switching-off Submodule (Pattern 3)

The equivalent circuit is similar to Fig. 20(b), thus

$$Z_{\text{Switching-off}}^{\text{Pattern_3}} \approx Z_{\text{Switching-off}}^{\text{Pattern_2}}. \quad \text{(A.6)}$$

REFERENCES

[1] A. Lesnicar and R. Marquardt, “An innovative modular multilevel converter topology suitable for a wide power range,” in *Proc. IEEE Bologna Power Tech Conf. Proc.*, 2003, p. 6.

[2] M. A. Perez, S. Bernet, J. Rodriguez, S. Kouro, and R. Lizana, “Circuit topologies, modeling, control schemes, and applications of modular multilevel converters,” *IEEE Trans. Power Electron.*, vol. 30, no. 1, pp. 4–17, Jan. 2015.

[3] S. Debnath, J. Qin, B. Bahrani, M. Saeedifard, and P. Barbosa, “Operation, control, and applications of the modular multilevel converter: A review,” *IEEE Trans. Power Electron.*, vol. 30, no. 1, pp. 37–53, Jan. 2015.

[4] Y. Tian, X. Yang, and W. Chen, “A novel copper layer-based field-to-trace coupling model and EMS evaluation method for DSP-based control circuit in MMC-HVDC system,” *IEEE J. Emerg. Sel. Topics Power Electron.*, vol. 9, no. 1, pp. 1133–1146, Feb. 2021.

[5] R. Zhu, N. Lin, V. Dinavahi, and G. Liang, "An accurate and fast method for conducted EMI modeling and simulation of MMC-based HVdc converter station," *IEEE Trans. Power Electron.*, vol. 35, no. 5, pp. 4689–4702, May 2020.
[6] Y. Tian, W. Chen, A. Zhou, and X. Yang, "Near-field radiation EMS research for driver PCB in MMC-HVDC system: A novel copper layer based EMI coupling model," in *Proc. IEEE Appl. Power Electron. Conf. Expo.*, 2020, pp. 2736–2740.
[7] X. Chen, W. Chen, Y. Han, Y. Sha, X. Yang, and X. Li, "Common-mode interference study of a auxiliary power supply based on the serialization of SiC MOSFETs for MMC-HVDC system," in *Proc. IEEE 8th Int. Power Electron. Motion Control Conf.*, 2016, pp. 31–36.
[8] Z. Bin, C. Wenjie, H. Lang, Z. Jiao, and Y. Xu, "Modeling and analysis of conducted EMI for a modular multilevel converter," in *Proc. 9th Int. Conf. Power Electron.*, 2015, pp. 268–273.
[9] F. Wang, J. Liu, and X. Wang, "Analysis of conducted EMI for sub-modules in modular multilevel converter," in *Proc. IEEE Int. Conf. Inf. Technol., Big Data Artif. Intell.*, 2020, pp. 1348–1353.
[10] M. Liu, J. Liu, and X. Wang, "An intuitive and accurate EMI model for a modular multilevel converter," in *Proc. IEEE Int. Conf. Inf. Technol., Big Data Artif. Intell.*, 2020, pp. 1337–1342.
[11] Y. Liang, J. Dong, W. Sun, and J. Chen, "MMC modeling and internal electromagnetic interference mechanism analysis," in *Proc. IEEE 1st Int. Power Electron. Appl. Symp.*, 2021, pp. 1–6.
[12] T. Sun, X. Pei, Y. Shan, P. Zhou, J. Yan, and J. Pei, "A fast modeling method for EMI sources in MMC based on nearest level modulation and capacitor voltage sorting algorithm," in *Proc. IEEE 12th Energy Convers. Congr. Expo.—Asia*, 2021, pp. 1015–1020.
[13] J. Chen et al., "A comprehensive analysis of voltage to ground of floating submodule for MMC," in *Proc. 21st Eur. Conf. Power Electron. Appl.*, 2019, pp. P.1–P.9.
[14] T. Sun and X. Pei, "Comparison analysis on EMI sources of MMC under NLM and PSC-PWM strategies," in *Proc. IEEE 4th Workshop Electron. Grid*, 2019, pp. 1–4.
[15] J. Wang, H. Li, Z. Yang, and B. Zhang, "Common-mode voltage reduction of modular multilevel converter based on chaotic carrier phase shifted sinusoidal pulsewidth modulation," in *Proc. IEEE Int. Symp. Electromagn. Compat. Signal/Power Integr.*, 2020, pp. 626–631.
[16] H. Li, J. Wang, and Z. Yang, "Common-mode voltage reduction of modular multilevel converter based on six-segment carrier level shifted sinusoidal pulsewidth modulation," in *Proc. IEEE 9th Int. Power Electron. Motion Control Conf.*, 2020, pp. 807–811.
[17] J. Chen, D. Jiang, W. Sun, and X. Pei, "Common-mode voltage reduction scheme for MMC with low switching frequency in AC-DC power conversion system," *IEEE Trans. Ind. Inform.*, vol. 18, no. 1, pp. 278–287, Jan. 2022.
[18] Y. Shan, X. Pei, T. Sun, P. Zhou, M. Zhang, and L. Zhou, "Space spread-spectrum-based PSC-PWM for MMC to reduce conducted CM EMI," in *Proc. IEEE 12th Energy Convers. Congr. Expo.—Asia*, 2021, pp. 1916–1921.
[19] Y. Shan, X. Pei, T. Sun, M. Zhang, P. Zhou, and D. Jiang, "Space spread-spectrum strategy for MMC to reduce the conducted EMI," *IEEE Trans. Ind. Electron.*, vol. 69, no. 11, pp. 10807–10818, Nov. 2022.
[20] Z. Wang et al., "A review of EMI research in modular multilevel converter for HVDC applications," *IEEE Trans. Power Electron.*, vol. 37, no. 12, pp. 14482–14498, Dec. 2022.
[21] A. R. Hefner and D. M. Diebolt, "An experimentally verified IGBT model implemented in the Saber circuit simulator," *IEEE Trans. Power Electron.*, vol. 9, no. 5, pp. 532–542, Sep. 1994.
[22] A. R. Hefner, "Analytical modeling of device-circuit interactions for the power insulated gate bipolar transistor (IGBT)," *IEEE Trans. Ind. Appl.*, vol. 26, no. 6, pp. 995–1005, Nov./Dec. 1990.
[23] K. Sheng, B. W. Williams, and S. J. Finney, "A review of IGBT models," *IEEE Trans. Power Electron.*, vol. 15, no. 6, pp. 1250–1266, Nov. 2000.
[24] M. J. Nave, "Prediction of conducted emissions in switched mode power supplies," in *Proc. IEEE Int. Symp. Electromagn. Compat.*, 1986, pp. 1–7.
[25] D. Zhang, D. Chen, and D. Sable, "Non-intrinsic differential mode noise caused by ground current in an off-line power supply," in *Proc. IEEE Rec. 29th Annu. Power Electron. Specialists Conf.*, 1998, pp. 1131–1133.

Tao Sun was born in Jiangxi Province, China, in 1996. He received the B.S. degree in electrical engineering and automation from the School of Electrical and Electronic Engineering, North China Electric Power University, Beijing, China, in 2018. He is currently working toward the Ph.D. degree in electrical engineering with the Huazhong University of Science and Technology, Wuhan, China.

His research interests include the modeling and suppression methods of EMI in power electronic converters.

Xuejun Pei (Senior Member, IEEE) received the B.E., M.E., and Ph.D. degrees in electrical engineering from the Huazhong University of Science and Technology, Wuhan, China, in 1998, 2001, and 2004, respectively.

In 2004, he joined the Huazhong University of Science and Technology, as a Teaching Assistant. Since 2006, he has been a Full Professor with the College of Electrical and Electronic Engineering. His research interests include high-power converter, EMC issue, fault diagnosis of power electronics, and the related application in the power system.

Yue Shan was born in Changchun, Jilin Province, China, in 1996. He received the B.S. degree in electrical engineering and automation from the Chongqing University, Chongqing, China, in 2019. He is currently working toward the M.S. degree in electrical engineering with the Huazhong University of Science and Technology, Wuhan, China.

His research interests include electromagnetic compatibility of the power converter.

Jian'guo Pei received the B.S. degree in hydropower engineering from the School of Hydropower and Information Engineering, Huazhong University of Science and Technology, Wuhan, China, in 2018. He is currently working toward the M.S. degree with the School of Electrical and Electronic Engineering, Huazhong University of Science and Technology, Wuhan, China.

His research interests include the application and stability study of power electronic technology in power quality control.

Dong Jiang (Senior Member, IEEE) received the B.S. and M.S. degrees in electrical engineering from the Tsinghua University, Beijing, China, in 2005 and 2007, respectively, and the Ph.D. degree in power electronics and motor drives from the University of Tennessee, Knoxville, TN, USA, in 2011.

He was with the United Technologies Research Center, East Hartford, CT, USA, as a Senior Research Scientist/Engineer, from January 2012 to July 2015. He has been with the Huazhong University of Science and Technology, Wuhan, China, as a Professor, since July 2015. He has authored/coauthored more than 100 IEEE journal and conference papers. His research interests include power electronics and motor drives.

Prof. Jiang was the recipient of six best paper awards in IEEE conferences. He is an Associate Editor for the IEEE TRANSACTIONS ON INDUSTRY APPLICATIONS.